**Doubly Differential Reactive Scattering
In Molecular Penning Ionization Systems**

by

Keerti Gulati

B.Sc , Kota University , Rajasthan , India

M.Sc, Kota University , Rajasthan, India

Submitted to the Graduate Faculty of

University of Pittsburgh in partial fulfillment

of the requirements for the degree of

Masters Of Science (M.S.)

University of Pittsburgh

2005

UNIVERSITY OF PITTSBURGH

FACULTY OF ARTS AND SCIENCES

This dissertation was presented

by

Keerti Gulati

It was defended on

Aug, 2005

and approved by

Dr. Peter Siska

Dr. Ken Jordan

Dr. Michael Golde

Dr. Peter Siska
Dissertation Director

DOUBLY DIFFERENTIAL REACTIVE SCATTERING
IN MOLECULAR PENNING IONIZATION SYSTEMS

Keerti Gulati, MS

University of Pittsburgh, 2005

The Penning Ion Angle Energy Distribution (PIAED) technique was used to study reactive scattering involving a molecular target (H_2) and an electronically excited noble gas (He). Crossed molecular beam setup was used to ensure single collision events, so that information on the newly formed products could be obtained without the averaging effects of secondary collisions. Optical quenching of one of the two metastable states was employed to perform state selected measurements.

TABLE OF CONTENTS

LIST OF TABLES

LIST OF FIGURES

1.   INTRODUCTION

Dynamics is the description of the motion under the influence of a force (or a potential)[1]. Thus, molecular dynamics deals with the mechanism of elementary physical and chemical processes at a molecular level and this assists in the interpretation of many macroscopic rate processes. [2]

One of the most direct means of probing molecular dynamics is the crossed molecular beams method. This technique involves observing the scattering of two colliding particles as a result of their interaction under single collision conditions, eschewing the averaging effects of secondary collisions. Also, molecular beams provide a well defined reagent beam direction, establishing a coordinate system, which is ideal for angle- and -energy distribution measurements of the scattered products. Supersonic molecular beams, in particular, have advanced reaction dynamics even further, by virtue of their narrow velocity distribution, high number density and high center line velocity.

The greatest promise of molecular beams is to unravel the potential energy surface[3] which contains all the information needed to understand reactivity. Results obtained for the non-reactive ground electronic state species are found to be consistent with the potentials that had been deduced approximately, from temperature-dependent transport coefficients, second virial coefficients and liquid and solid state properties, where available. Fewer studies have been carried out with electronically excited atoms or molecules, making excited state chemistry a

fertile field of study. Another motivation in the study of excited noble gas chemistry is the extremely reactive nature of the rare gas atoms in their lowest lying metastable excited states, in contrast to their inertness in the ground states.4 Being optically forbidden, by the electric dipole selection rules, to radiatively decay to the ground state, these species have lifetimes much longer (>20 ms) than transit times of atoms in a typical high-vacuum apparatus. The rare gas metastables arise from the excitation of an electron from the closed shell to the lowest unoccupied s orbital. Some important properties of these species are listed in Table 1-1.

Table 1.1: Excitation Energies and Lifetimes of Noble Gas Metastables.

Atom	Metastable State	Excitation Energy	Radiative Lifetimes (s)
Helium	2^1S	20.616	1.95×10^{-2}
	2^3S	19.820	7.9×10^{3}
Neon	$^3P_0$	16.716	4.3×10^{2}
	$^3P_2$	16.619	2.44×10^{1}
Argon	$^3P_0$	11.723	4.49×10^{1}
	$\mathbf{^3P_2}$	11.548	5.59×10^{1}
Krypton	$^3P_0$	10.563	4.9×10^{-1}
	$^3P_2$	9.915	8.51×10^{1}
Xenon	$^3P_0$	9.447	7.8×10^{-2}
	$^3P_2$	8.315	14.95×10^{1}

Table 1.2: Ionization Potentials[14] and Polarizabilities[16] of Noble Gas Metastables

Atom	Metastable State	Ionization Potential	Polarizability (Å^3)
He	2^1S	3.972	118.9
	2^3S	4.768	48.6
Ne	$^3P_0$	4.849	…..
	$^3P_2$	4.946	27.8
Ar	$^3P_0$	4.036	…..
	$\mathbf{^3P_2}$	4.211	47.9
Kr	$^3P_0$	3.437	…..
	$^3P_2$	4.084	50.7
Xe	$^3P_0$	2.683	…..
	$^3P_2$	3.815	63.6

Table 1-2 compares the values of ionization potentials and polarizabilities for the metastable noble gases with the corresponding alkali metals. The closeness in the values stems from the similarity in both electronic structure and reactivity of the metastables and the alkali metals.

An excited state, A^*, can be deexcited by collision through many channels, which may be accompanied by excitation, dissociation or ionization of the target molecule BC. Ion production may result from the following processes:

$$A^* + BC \rightarrow A + BC^+ + e^- \qquad \text{(Penning Ionization)} \qquad \text{(1a)}$$
$$A^* + BC \rightarrow ABC^+ + e^- \qquad \text{(Associative Ionization)} \qquad \text{(1b)}$$
$$\rightarrow A + B^+ + C + e^- \qquad \text{(Dissociative Ionization)} \qquad \text{(1c)}$$
$$\rightarrow AB^+ + C + e^- \qquad \text{(Rearrangement Ionization)} \qquad \text{(1d)}$$
$$\rightarrow A + B^+ + C^- \qquad \text{(Ion pair production)} \qquad \text{(1e)}$$
$$\rightarrow A^+ + BC^- \qquad \text{(Ion pair production)} \qquad \text{(1f)}$$
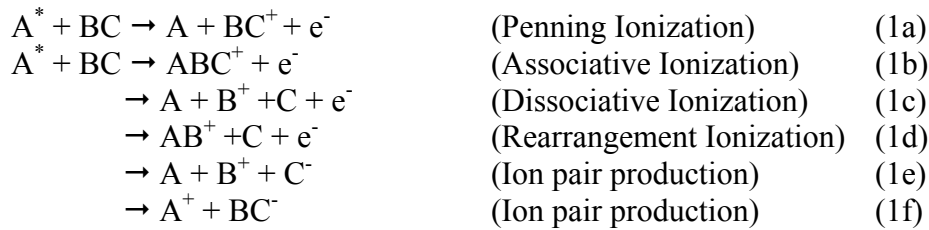
These ionizing reactions are collectively referred to as chemionization, the field of our work. The channels open for a relaxing excited entity are determined by energetics; dynamics govern the branching among them.

Penning Ionization(PI) (1a) occurs only when the excitation energy of the metastable rare gas exceeds the ionization potential of its target. The process was first postulated by Frans M. Penning in 1927. He was studying the breakdown voltages in gas discharges, when he found that impurities caused the voltage required to decrease—rare gas metastables, formed in the process, were ionizing the impurities.

Penning Ionization(1a), and also reactions (1b), (1c) and 1(d) can be viewed as passing through two collision intermediates or "transition states",

$$A^* + BC \underset{a'}{\overset{a}{\rightleftharpoons}} [ABC]^* \overset{b}{\rightarrow} [ABC]^+ + e^-$$

$$\xrightarrow{c} \text{Ionic products.}$$
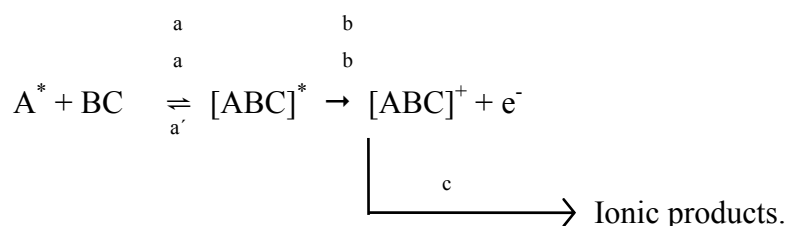
The departing electron can sometimes carry away enough energy to leave the products bound, resulting in associative ionization(1b).

It is generally accepted that PI is an electron transfer process[5] where the ejected Penning electron originates from the electronically excited species.[34] The alternate, radiative mechanism, in which a radiative relaxation of the excited species, is followed by a absorption of the photon by the target to achieve ionization. But spin-polarization measurements[6] support the exchange mechanism according to which a valence electron of the target is transferred into the hole in the rare gas core, with simultaneous ejection of the excited electron. Both mechanisms are illustrated in Figure 1.1.
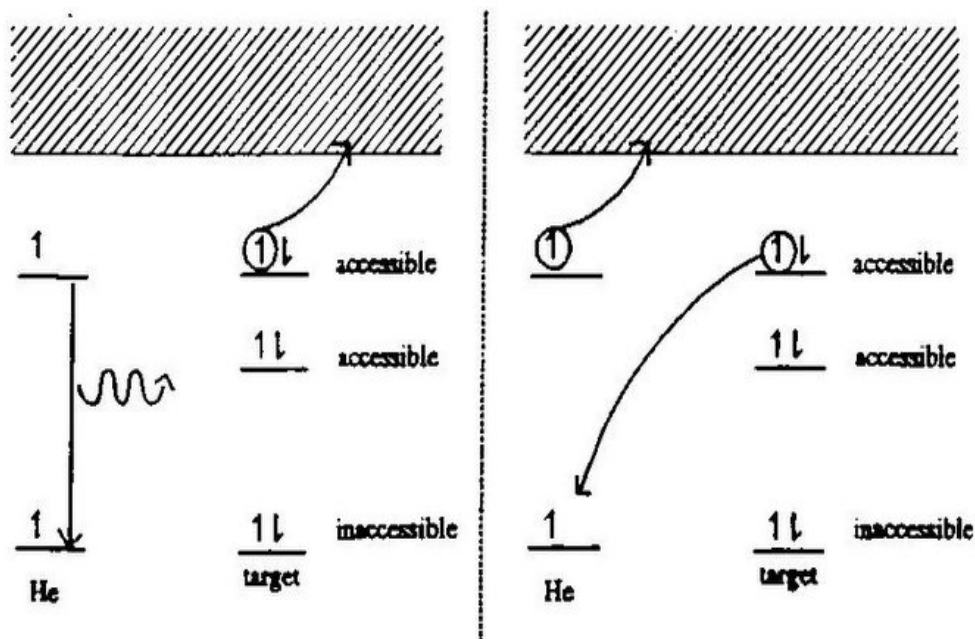
Figure 1.1 : Radiative (left panel) and exchange (right) mechanisms for Penning Ionization.

Detection and analysis of the scattered metastables as a function of collision energy yields powerful information regarding the PI dynamics. For example, the presence of a short range local minimum [7-11] in the 2^1S, but not the 2^3S potentials was the result of such studies. Penning electrons may be studied, which harvest nascent vibronic distributions of the Penning ions; Penning ionization electron spectroscopy (PIES) is often viewed as a transition state spectroscopy. Measurements on the Penning ions include some of the earliest crossed molecular beam experiments of Penning ionization(late 1960's) which determined the total quenching rate constant k_Q of various Penning systems[12]. The total ionization cross sections and their velocity

and mass-dependencies have been measured for a number of atomic systems. The Siska group has pursued all these areas studying primarily He^* and Ne^* with a variety of different targets.

The Penning Ion Angle Energy Distribution (PIAED) technique has been used in the present work to study the reactive scattering, differential in both product ion scattering angle (PIAD) and product ion scattering energy(PIED). These results provide insight into the post-ionization dynamics. The first doubly differential Penning reaction cross section measurement was done in 1981 by Khan, Siddiqui and Siska. Longley[13] has recently (1995) measured at four other atomic systems, doubly differential cross section $\sigma(\theta, E')$, where E' is the kinetic energy of the product ions.

The focus of this work is to extend the atomic PIAED studies to molecular Penning systems (involving a molecular target). Currently the $He^*(2^{1,3}S) + H_2$ system is being studied; it is a prototype for molecular PI studies, both because of its simplicity(which enables much more rigorous theoretical studies to be done) and because of the strong base provided by previous studies.

The total ionization cross sections have been measured by several groups[5] to be close to $2Å^2$ for He^* $(2^1S)+$ H_2 and $1Å^2$ for He^* (2^3S) at E = 1.6 kcal/mol. The collision energy dependance of total ionization cross section has been determined by Martin et.al [10, 11]. Non-reactive scattering experiments[10] have provided anisotropic interaction potentials through an optical model analysis of the angular distributions I(θ). A complete PIES study of this system has recently been reported by Bevsek et.al[17]. Preliminary results of a PIAED study of He^* $(2^{1,}$ $^3S)+$ H_2 are reported here. An introduction to scattering theory and the classical theory of PI is given (Chapter II), followed by a review of the kinematics applied to reactive scattering systems (Chapter III). Chapter IV entails a description of the apparatus and the data acquisition procedure

employed. Analysis and discussion of the results to date and plans for future work are given in Chapter 5 and 6.

2. THEORY

The theoretical basis for the experimental measurements will be discussed presently to aid in physical understanding. It must be noted, however, that theory lags behind experiment in the area of molecular targets, since current PI theories treat atoms only. Theoretical descriptions of PI dynamics were developed by Nakamura[18] and Miller[19], which are based, primarily, on the potential curve model of PI that we describe here.

PI results, if in a system $A^* + B$, the excitation energy E of the metastable A^* exceeds the ionization potential IP of the target B. Figure 2-1 shows the incoming reactant channel potential $V_0(r)$, which lies in the ionization continuum of the outgoing channel potential $V_+(r)$. PI occurs by auto-ionizing transitions between these two potential curves, $V_0(r)$ and $V_+(r)$, which are asymptotically separated by ε_0 where

$$\varepsilon_0 = E(A^*) - IP[B(n', v')] \tag{2a}$$

Where $IP[B(n', v')]$ is the ionization potential to a specific electronic and vibrational state of the target ion B^+ (rotational states will not be discussed since they are typically not resolved in PIAED).

$V_+(r)$ is actually the lower bound of the electronic continuum. So PI occurs through a resonance of $V_0(r)$ and a subset of this continuum, the leakage being governed by an ionization width $\Gamma(r)$. The exchange mechanism postulates PI to occur through an orbital overlap, so $\Gamma(r)$ decreases exponentially with r as shown in the figure. Thus the reactants A^* and B continue to
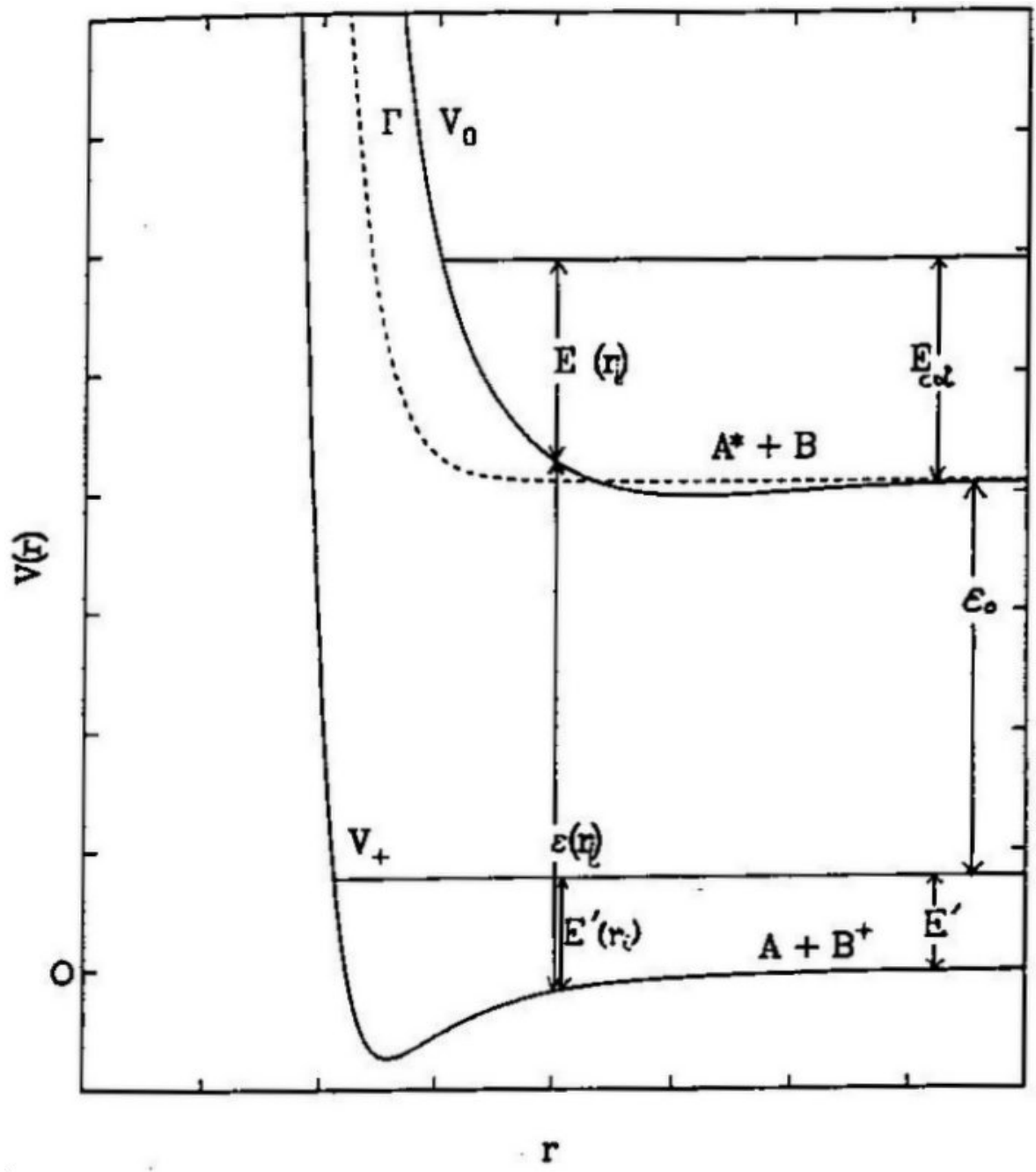
Figure 2.1: Two State Potential Curve Model of PI

travel along the potential energy surface V_o until this coupling is strong enough to cause a vertical Franck-Condon type (within the Born-Oppenheimer approximation), irreversible transition at the rate of $\Gamma(r)/\hbar$ with simultaneous ejection of an electron.[20]

For a transition occurring at internuclear separation r_i, the kinetic energy carried away by the departing electron is given by

$$\epsilon(r_i) = V_o(r_i) - V_+(r_i) \tag{2b}$$

Conservation of energy dictates that

$$E_T = V_0(r_i) + E(r_i) = V_+(r_i) + \epsilon(r_i) + E'(r_i) \tag{2c}$$

where E_T is the total energy, and $E(r_i)$ and $E'(r_i)$ are the local and asymptotic kinetic energies of the reactants and products, respectively at r_i. Also from energy conservation,

$$E_T = E' + \epsilon(r_i) = E_{col} + \epsilon_o$$

where E' and E_{col} are the asymptotic kinetic energy of products and reactants respectively. Depending on the kinetic energy carried away by the Penning electron, the kinetic energy of the products can be greater or smaller than zero:

$$E'(r_i) < 0 \quad \text{if} \quad \epsilon(r_i) > V_0(r_i) - V_+(r_i) + E(r_i) \tag{2d}$$

$$E'(r_i) > 0 \quad \text{if} \quad \epsilon(r_i) < V_0(r_i) - V_+(r_i) + E(r_i) \tag{2e}$$

A negative product kinetic energy predicts that the collision partners cannot separate, resulting in associative ionization while condition (2e) corresponds to PI.

The potential curve model of PI described above, works very well in understanding the energies of PI and AI; the dynamics of PI scattering can be interpreted by a knowledge of classical scattering theory discussed below.

The total energy E_T possessed by the colliding particles is conserved throughout the collision,

$$E_T = \text{constant} \tag{2f}$$

In the course of collision E_T gets partitioned into, kinetic and potential energy terms in the course of a collision,

$$E_T = K(r) + V(r) \tag{2g}$$

where $K(r)$ is the local relative kinetic energy at separation r and $V(r)$ is the potential energy, which is equal to zero, when the particles are well separated. r is the interparticle relative separation.

If we express the kinetic energy as being comprised of a radial and an angular component then equation (2g) may be written as

$$E_T = \frac{1}{2}\mu(\dot{r})^2 + \frac{1}{2}\mu(\dot{r})^2\,(\dot{\theta})^2 + V(r) \tag{2f}$$

(dot designates the time derivative) Thus, $\dot{r}$ is the speed at which colliding particles approach each other, θ is the scattering angle (Figure 2-2), $\dot{\theta}$ is the angular speed for rotation of r, and μ is the reduced mass $(m_1 m_2)/(m_1 + m_2)$.

The first term in the above equation is the radial kinetic energy due to the component of velocity along the line of centers of the colliding partners. The second term gives the centrifugal energy, that is, kinetic energy due to component of velocity perpendicular to the line of centres of collision partners. A simple classical trajectory, in the center of mass system, illustrating these quantities is shown in Figure 2-2[21], describing the trajectories of a collision in the absence and presence of an interparticle force field.

The impact parameter b, may now be introduced, which is defined as the distance of closest approach between the two colliding particles, provided no forces acted on them.[1] It is, thus, a

measure of closeness of a collision. The turning point of a collision, r_c, may be defined as the smallest inter-nuclear distance, and the deflection angle χ is the angle between the final relative velocity vector v' and the initial value v. Since the classical trajectories are symmetric about the scattering at the turning point, so the deflection angle may be expressed as,

$$\chi \ = \ \pi \ - \ 2\theta_c \tag{2g}$$

The rotation of the collision partners accumulates centrifugal energy, which leaves less radial kinetic energy to overcome the repulsive wall of V(r) to penetrate to smaller r. The centrifugal energy, therefore, acts as a barrier, or a repulsive contribution to V(r). Hence we can define an effective potential V_{eff} (r), which incorporates this centrifugal barrier,

$$V_{eff}(r) = \ \frac{E_T b^2}{r^2} + V(r) \tag{2h}$$

Qualitatively, for larger b, less radial KE is available to penetrate the smaller r, so the turning point on V(r) moves outward to larger internuclear distances. As a consequence, the centrifugal barrier affects the amount of Associative Ionization that takes place. This effect is portrayed in the potential curves of Figure 2-3[3] drawn as a function of collision angular momentum (L). As L increases, the repulsive centrifugal contribution flattens out the well, until the curve becomes purely repulsive, as in the curve corresponding to L_5. And since AI results from $[AB^+]$ being trapped inside this well, no AI will happen when impact parameter is too large.

The centrifugal term (second term) in equation (2f) may also be expressed as,

$$\frac{1}{2}\mu r^2 \ \dot{\theta}^2 \ = \frac{E_T b^2}{r^2} \tag{2i}$$

As a result
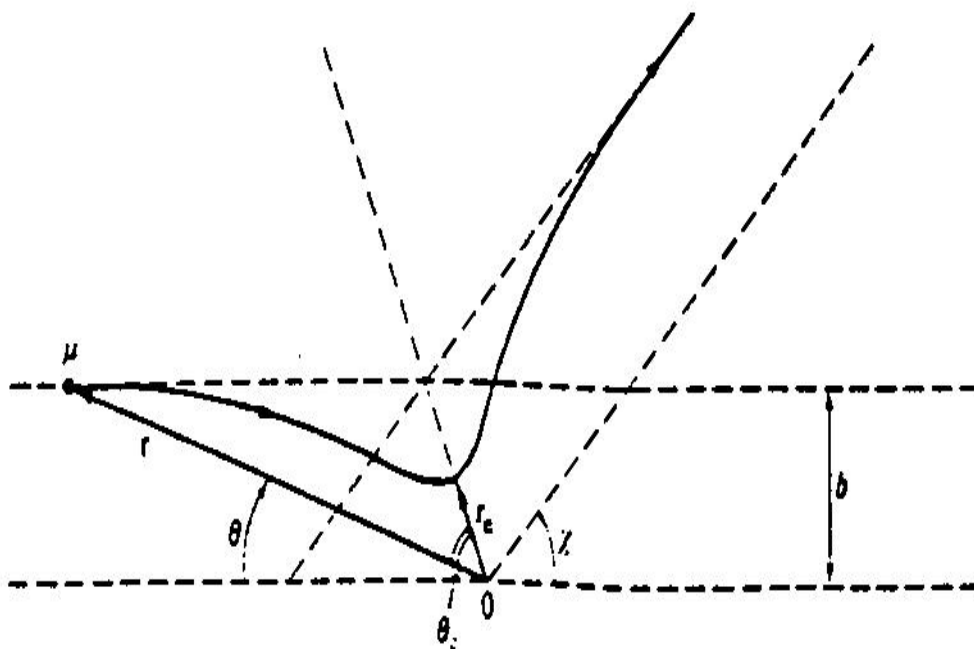
μ = reduced mass

r = internuclear distance

θ = scattering angle

r_c = turning point of the collision

θ_c = scattering angle corresponding to r_0

χ = deflection angle

b = impact parameter

Figure 2.2: Schematic classical trajectory

$$E_T = \frac{1}{2}\mu\dot{r}^2 + \frac{E_T b^2}{r^2} + V(r) \qquad\qquad (2j)$$

$$\dot{r} = \pm v\left[1 - \frac{b^2}{r^2} - \frac{V(r)}{E}\right]^{\frac{1}{2}} \qquad\qquad (2k)$$

The largest root of the above equation gives the turning point of the collision. The expression

for angular velocity $\dot{\theta}$, equation (2k) can be combined with the above equation to yield and

expression for θ as a function of r, which when integrated over the trajectory and evaluated at

the turning point yields the scattering angle at the turning point, θ_c.

$$\dot{\theta} = bv/r^2 \qquad\qquad (2l)$$

$$\theta_c = b\int_{r_c}^{\infty} \frac{dr}{r^2\left[1 - \frac{b^2}{r^2} - \frac{V}{E}\right]^{1/2}} \qquad\qquad (2m)$$

The correlation between deflection angle and initial impact parameter is called the deflection

function. Using equation (2g) the classical deflection function may be written as,

$$\chi(b, E) = \pi - 2b\int_{r_c}^{\infty} \frac{dr}{r^2\left[1 - \frac{b^2}{r^2} - \frac{V}{E}\right]^{1/2}} \qquad\qquad (2n)$$

Equation (2n) describes several features of the deflection function and the effects of

attractive and repulsive parts of V(r). For a given collision energy E_T, the figure demonstrates the

effect of different values of the impact parameter on the collision trajectory.

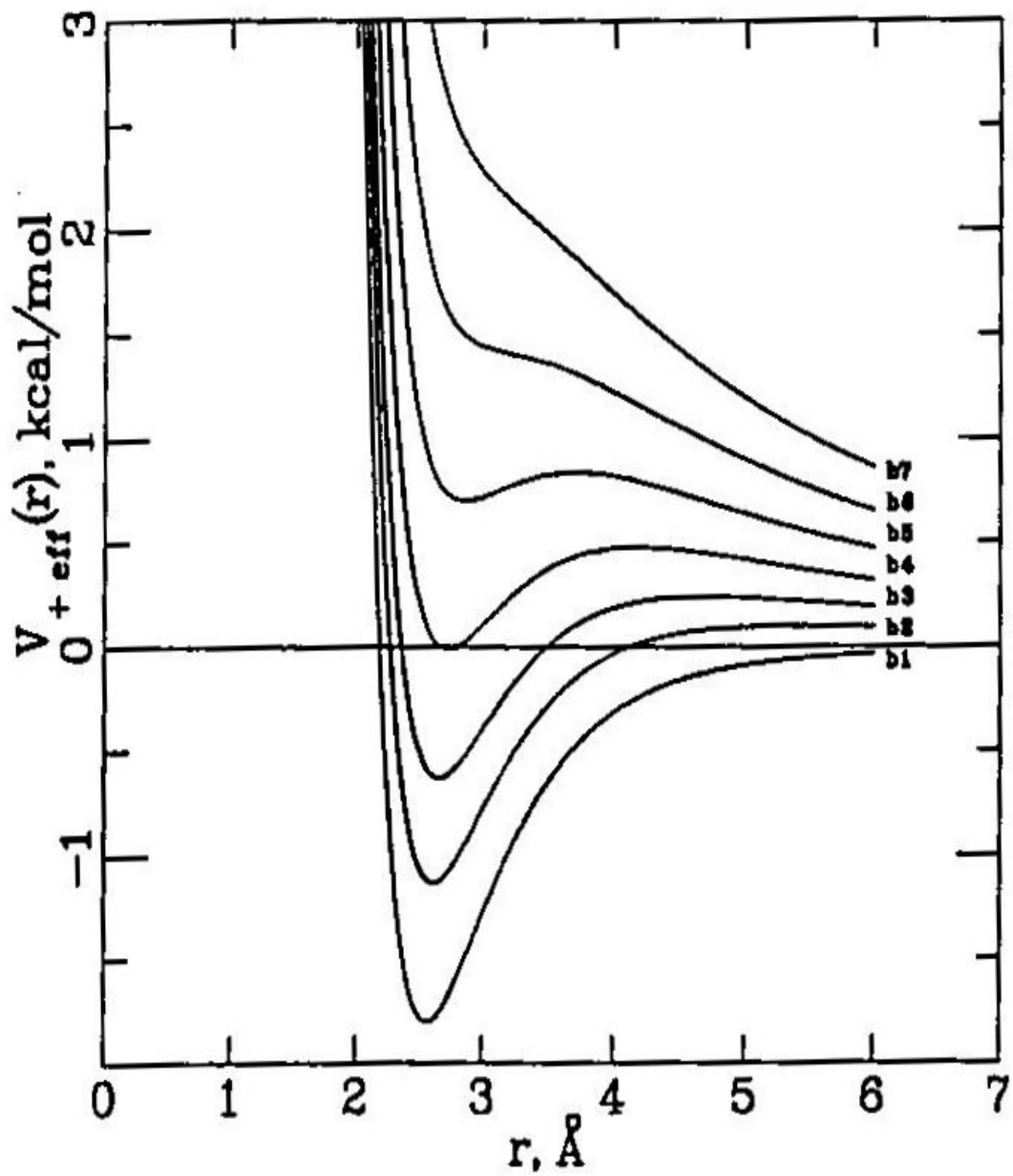For large values of b, the colliding species are too far away from each other to effect the

Figure 2.3: Schematic effective potentials illustrating effect of centrifugal energy on an attractive curve

original direction of approach and so the deflection angle is zero. As b decreases, the trajectories begin to sample only the long range attractive force, resulting in a negative deflection angle χ. The deflection angle continues to decrease with b until the rainbow impact parameter b_r. For values of b smaller than b_r the effect of repulsive force becomes dominant and the deflection angle increases and becomes zero when $b = b_g$, at the glory impact parameter, where the repulsive and attractive forces exactly cancel each other. As $b \rightarrow 0$, that is, for nearly head-on collisions, the molecules rebound in the backward direction. $(\chi \rightarrow \pi)$.

Equation (2n) works well for non-reactive two body scattering, but for a reactive system (such as PI), it must be modified since the trajectory would no longer be symmetric about the scattering angle at the turning point. Thus, an exact reactive formulation of $\chi(b, E)$ would require partitioning the collision into motion $V_o(r)$ and motion on $V_+(r)$, determining the appropriate deflection functions, and summing up the corresponding trajectories.

Collision cross section (σ) is defined as the area of a beam molecule as seen by a target molecule and vice versa. For collisions with impact parameters in the range b to b+db we have

$$d\sigma = 2\pi b db. \tag{2o}$$

The total collision cross section is then obtained by integrating over all values of b that result in a collision,

$$\sigma = \int 2\pi b db \tag{2p}$$

The reaction cross section, σ_R, is related to the collision cross section by the opacity function, P(b), which gives the reaction probability.

$$\sigma = \int_0^{b_{max}} 2\pi b P(b) db \tag{2q}$$

where b_{max} is the largest value of b for which reaction is still possible. The opacity function, P(b), is the fraction of collisions with impact parameter b, that lead to a reaction.

For collision trajectories with impact parameters in the range b to b+db, the final deflection angle χ lies in the range θ to θ+dθ, where θ= $|\chi|$. All these trajectories will enter via an annular cone, into a solid angle,

$$d\omega = 2\pi \sin\theta d\theta \tag{2r}$$

Also,

$$d\sigma_R = 2\pi bP(b)db = I(\theta) \, d\omega \tag{2s}$$

where I(θ)is the differential collision cross section. Thus,

$$I(\theta) \;=\; \frac{2\pi bP(b)db}{d\omega} = \frac{bP(b)}{\sin\theta \left|\dfrac{d\chi}{db}\right|} \tag{2t}$$

The correlation between b and χ is summarized again in figure 2-5. Also evident is the fact, that for $|\chi| < |\chi_r|$, three different values of b correspond to the same deflection angle θ= $|\chi|$, which increases the intensity observed at that θ. To account for this behavior, a modified form of equation (2t) is used in such a case,

$$I(\theta) \;=\; \sum_i \frac{b_i P(b_i)}{\sin\theta \left|\dfrac{d\chi}{db}\right|_i} \tag{2u}$$

The above relation implies, that at the glory impact parameter, where θ = 0°, a spike of infinite intensity should result, classically. A similar sin θ singularity is also expected as θ → 180°. However, since b is also approaching zero, the net ratio is constant. Hence, quantum damping of the classical spike occurs, yielding a peak at θ = 0°, referred to as a forward glory. Now at θ = 180° , whether or not a backward glory will appear, depends on the value of the

17

opacity function. If P(b) increases towards unity as b decreases, this will counteract the b: $\sin\theta$ ratio and a backward glory will appear. On the other hand, if P(b) is constant at a small b, no peak appears in the backward direction.

Equation (2t) may also be used to describe scattering intensity as a function of product velocity. This yields an expression for I(θ, E$'$) which is a doubly differential scattering cross section, differential in both scattering angle and recoil energy. For reactions such as Penning Ionization, products scattered at a given angle possess a distribution of velocities, corresponding to the range of internuclear distances over which ionization takes place. Hence product velocity analysis is essential to understand collision dynamics and so I(θ, E$'$) is a more powerful tool compared to I(θ) alone.

The scattering angle and product recoil velocity as discussed above are defined relative to the center of mass of the colliding molecules, but their measurement in the lab occurs in a space fixed coordinate system. Hence discussion on how the two types of observables are affiliated, is presented next.
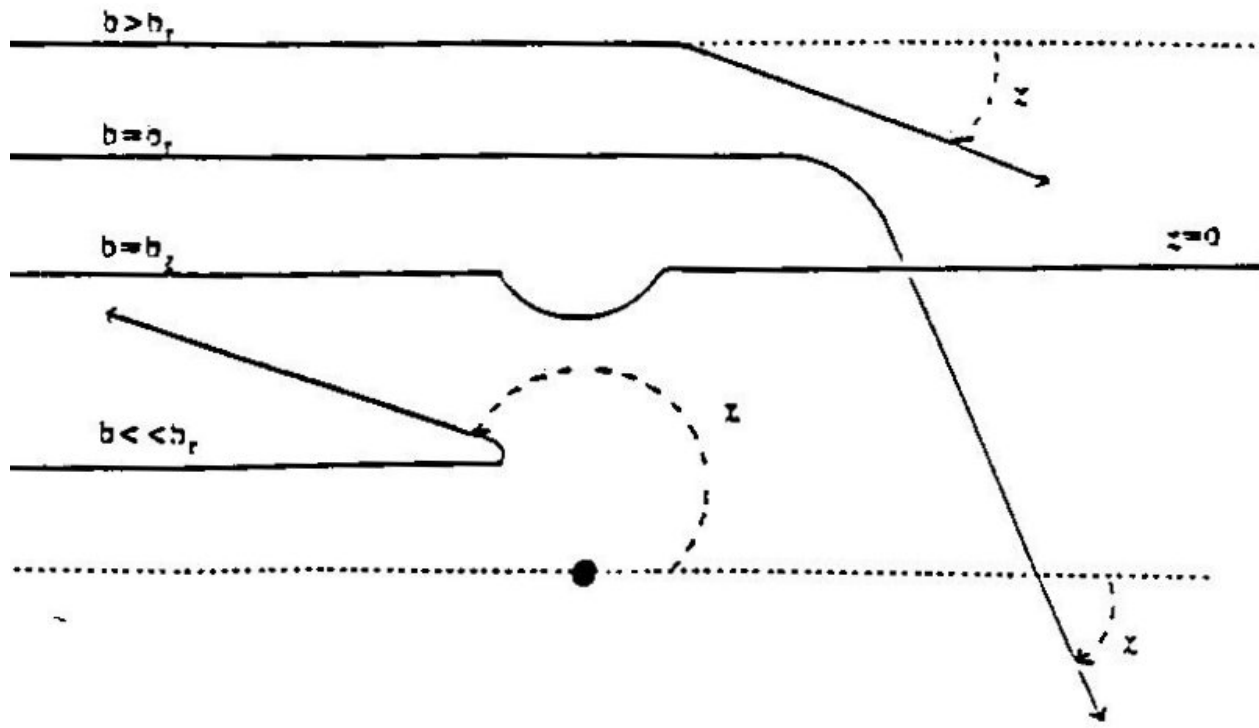
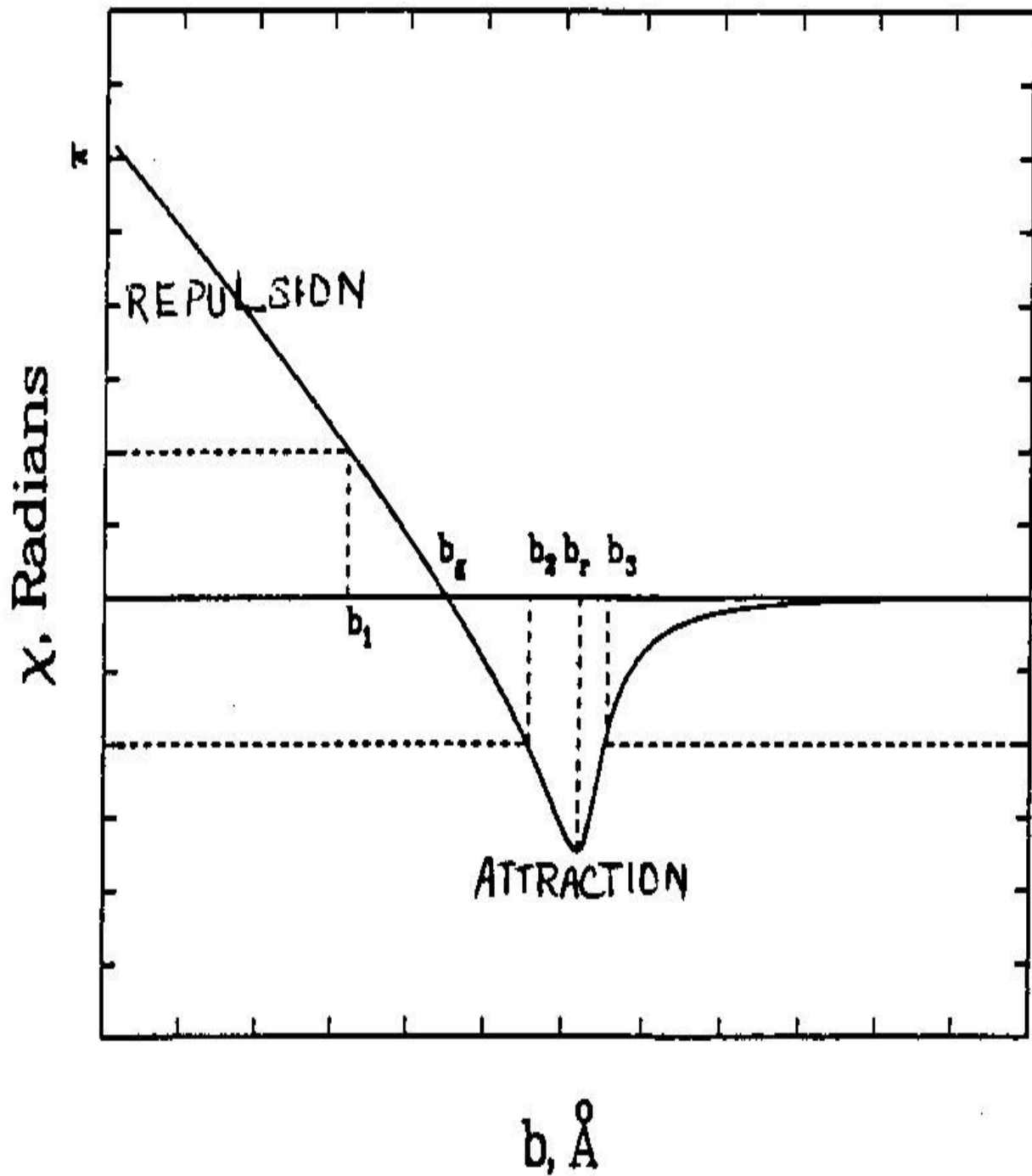**Figure 2.4: Collision trajectories at various impact parameters**

Figure 2.5: Typical deflection function at a given energy

3.   KINEMATICS.

The paths of two particles undergoing a collision in space can be described using six scalar coordinates as a function of time. However the inter-particle force depends only on the relative separation r between the colliding particles. So it is most convenient to describe the collision in center-of-mass (CM) frame, using fewer degrees of freedom. The CM (called the centroid) remains unchanged throughout the collision (if no external forces operate on the system) and so it can be subtracted from the total kinetic energy, which leaves us with the kinetic energy of relative motion. Thus a CM frame provides a coordinate system in which the CM of colliding molecules is at rest and the reaction dynamics is described solely in terms of relative motion of colliding molecules.

On the other hand, the experimental measurements of the scattering angle and product recoil velocity, are made by measuring the detector angle relative to some fixed point in the lab-based (LAB) coordinate system. Since the CM coordinate system is moving with respect to the LAB frame, this may distort experimentally measured lab observations. Hence, to fully understand the experimental scattering data and make meaningful comparisons to calculated properties, a LAB → CM coordinate transformation is employed[22]. This is most explicitly pictured with the help of a "vector velocity" or "Newton" diagram (Figure 3-1), which is a vector diagram of particle velocities both before and after the collision.

The relative velocity of two colliding particles, is simply the difference,

$$v = v_1 - v_2 \tag{3a}$$

where v_1 and v_2 are asymptotic LAB velocities of $1°$ beam of mass m_1 and a $2°$ beam of mass m_2 respectively. The velocity of center of mass is

$$C = \frac{m_1 \ v_1 + m_2 v_2}{m_1 + m_2} \tag{3b}$$

If u_1 and u_2 denote the CM velocities of the $1°$ and $2°$ beams respectively, then the relation between the LAB and CM velocities is

$$u_1 = v_1 - C \tag{3c}$$

$$u_2 = v_2 - C \tag{3d}$$

The Newton diagram portrays the correlation between all these parameters. The primed quantities in the figure refer to the collision products. The relative velocity vector v is the path along which the two particles travel towards each other to collide at the tip of the centroid vector C. In elastic scattering, CM translational energy remains unchanged. Hence as a result of this collision, v rotates about the centroid tip through the CM deflection angle θ, while the magnitude of v is conserved. Thus, although $u_1 = u_1'$ for elastic scattering, v_1' that is the LAB product velocity, changes as a function of θ.

In the case of inelastic scattering, internal $\leftrightarrow$ translational energy exchange may occur and so v may undergo a change in both magnitude and direction.

For reactive scattering, v may be rotated through some θ (Figure 3-1), as well as change its magnitude. Further, the centroid tip may partition v' in a different way than v, if the products formed have a different mass ratio than the reactants.
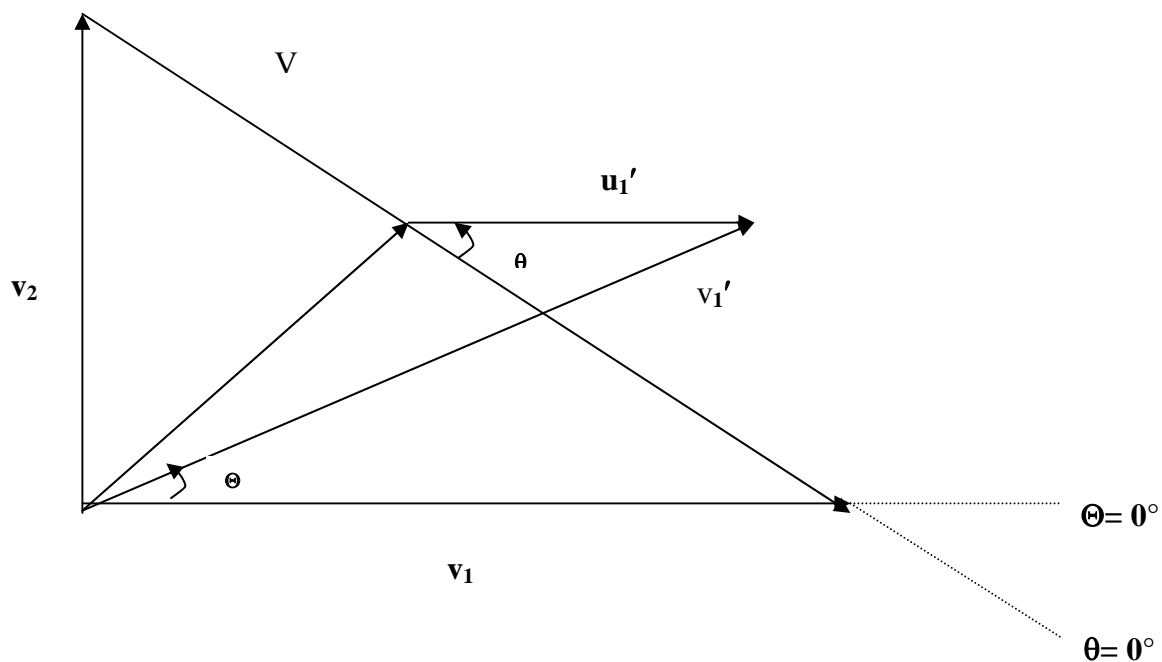
v_1	=	initial LAB velocity of particle 1
v_2	=	initial LAB velocity of particle 2
v	=	initial relative velocity of reactants
C	=	center of mass (centroid) vector
Θ	=	LAB deflection angle of particle 1
θ	=	CM deflection angle of particle 1
v_1'	=	LAB recoil velocity of particle 1
u_1'	=	CM recoil velocity of particle 1

Figure 3.1 : Newton Diagram for reactive scattering.

The Jacobian factor that relates the LAB and CM coordinate systems may also distort lab observation of product ion intensity which, therefore, must be converted to CM intensity. The number of particles passing through a differential volume element per unit time must be the same in LAB and CM system,

$$I_{LAB}(\Theta, v)\, d\Omega dv = I_{CM}(\theta, u)\, d\omega du \tag{3e}$$

Where $d\Omega$ is the LAB solid angle of detection, dv the LAB differential velocity element and I_{LAB} the LAB product intensity. $d\omega$, du and I_{CM} are corresponding CM quantities. Since the LAB $\rightarrow$ CM transformation involves only translation and rotation of the axes, the volume elements in the velocity space of the two systems are equal, that is,

$$v^2 dv d\Omega = u^2 du d\omega \tag{3f}$$

Equation 3f applies to the special case of reactive scattering where the product velocities are continuous. This is the case in Penning Ionization, since ionization is possible over a continuous range of internuclear distances. The Jacobian of coordinate transformation is given by

$$\frac{d\omega du}{d\Omega dv} = \frac{v^2}{u^2} \tag{3g}$$

and thus LAB and CM intensities are related by

$$I_{CM}(\theta, u) = I_{LAB}(\Theta, v) \frac{u^2}{v^2} \tag{3h}$$

This expression suggests that as $u'\rightarrow 0$, CM intensity also approaches zero resulting in a valley of near zero intensity surrounding the centroid tip. A manifestation of this result is apparent in the CM velocity-angle contour plot discussed in Chapter V.

4.   EXPERIMENTAL

4.1.   APPARATUS.

The scattering experiments were performed in a crossed molecular beam vacuum chamber (inside dimensions 100cm x 100cm x 58cm) mounted on a rotatable lid. The apparatus has been described in a previous publication.[7] A schematic is presented in Figure 4-1.

The apparatus has five sub-chambers: two source chambers where supersonic expansion of each beam takes place, two buffer chambers where modifications to the beam are made, and the main chamber where collision and product detection occurs. Each of the chambers is served by its own vacuum system affecting differential pumping. The main chamber is pumped by a 10″ diffusion pump (Varian VHS-10) The metastable source is pumped by a 6″ diffusion pump(Varian VHS-6) while the target source by a 10″ diffusion pump(Varian VHS-10). The two buffer chambers are each served by a 4″ diffusion pumps (Varian VHS-4). These pumps are charged with silicon oil (DC 705 for the 10″ pumps and 704 for the 4″ and 6″ pumps). Each diffusion pump is backed by its own mechanical pump. Hand-wheeled gate valves help isolating the sub-chamber from its diffusion pump that allows for venting the apparatus without venting the diffusion pumps. Granville-Phillips ion gauges are used to monitor the sub chamber pressures.

A description of each sub-chamber and its characteristics is presented in detail below.

4.1.1.   1° AND 2° SOURCE CHAMBERS

Both the source chambers are engaged in production of supersonic beams which have wide applicability in studying microscopic chemical processes. The theory of supersonic beam production[28] is briefed below:

Production of supersonic beams requires a high pressure in the nozzle, usually on the order of thousands of torr. As a consequence, the mean free path of the stagnant gas inside the nozzle is much less than the nozzle orifice. Hence, the number of collisions occurring in the nozzle just before expansion is greatly increased. Nozzle collisions cause quenching of vibrations and rotations to the point of total relaxation which is called cooling. Because of energy conservation, the energy lost in vibrations and rotation is transferred to the translational energy beam flow. Thus the entire velocity distribution shifts to a higher velocity range. Since the internal degrees of freedom are cooled, this conforms to a beam with decreased motion and thus temperature. This beam with a lower temperature will thus have a narrow distribution, that too, at a higher velocity range.

The quality of a supersonic jet may be described by the translational temperature of the beam, T_{eff}, determined by,

$$T_{eff} = \frac{T_o}{1 + M^2 \left(\frac{\gamma - 1}{2} \right)} \qquad (4\text{-}1)$$
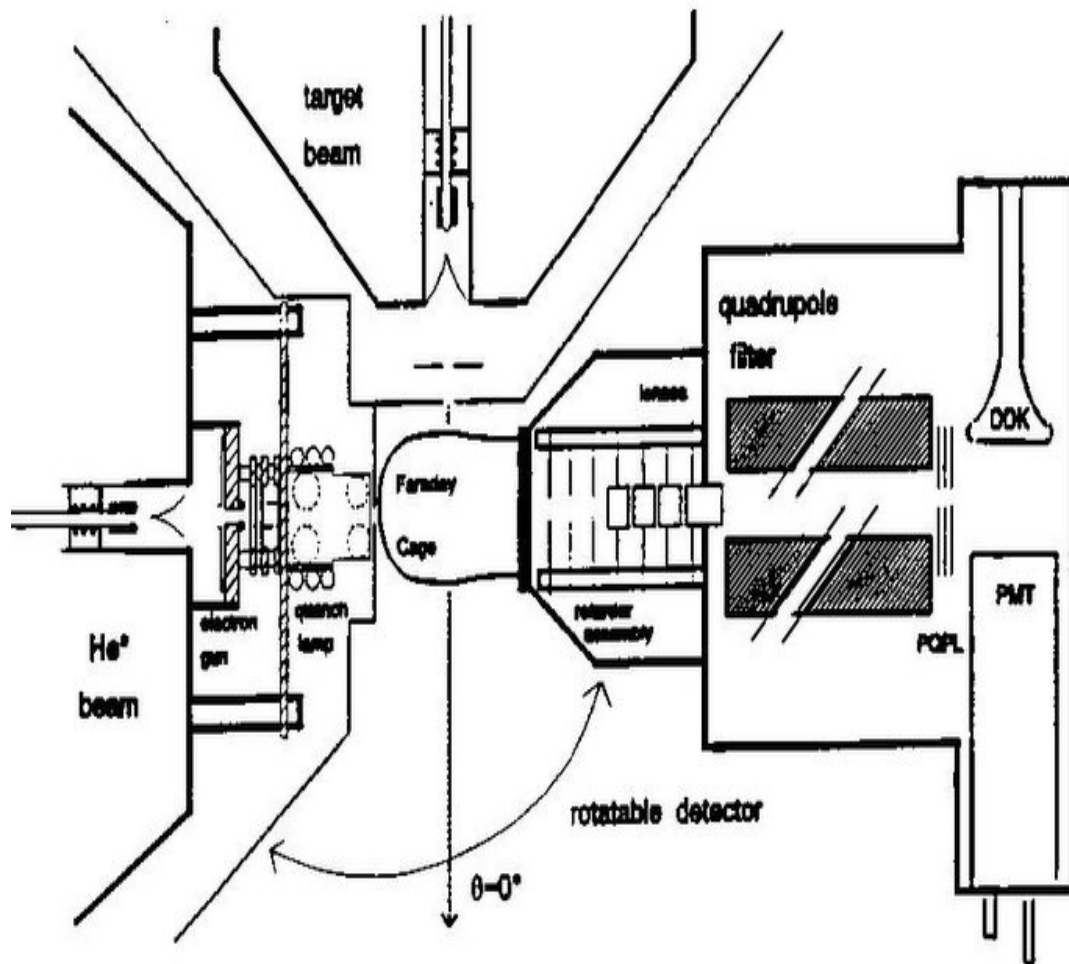
Figure 4.1: Schematic of the apparatus. Drawing is not to scale; refer to text for details.

Table 4.1: Time-Of-Flight[29] Expansion Parameters for He[*].

Nozzle Temperature, K	Mach Number	Peak Velocity (10^4 cm/sec)
312.4	17.65	17.682
348.0	17.68	18.16
395.4	16.05	19.34
440.4/	13.95	20.69
486.4	12.76	22.18
531.4	11.48	23.58
576.4	10.81	24.99
621.4	10.22	26.55
667.4	9.41	27.82
712.4	9.01	28.66
757.4	8.51	29.49
802.4	8.49	30.23
846.4	8.20	21.02
889.4	7.95	31.62
932.4	7.57	32.27
974.4	7.50	33.03
1014.4	7.05	33.57

where T_o is the temperature of the gas in the nozzle and M is the Mach number, v_f/u, which is the ratio of flow velocity to the local speed of sound. Typical Mach numbers for atomic supersonic beams often exceed 20, while molecular beams usually have M ~ 10. γ is the heat capacity ratio C_p/C_v of the expanding gas which is usually determined by time-of-flight (TOF) experiments; although a γ of 5/3 is often used for atomic gases (by equipartition theorem). TOF expansion parameters for He* are presented in Table 2-1 obtained from previous experiments[29].

Thus T_{eff} gives a measure of the degree to which the velocity distribution has been narrowed. The most probable beam velocity can be defined using T_{eff} by,

$$\alpha = \sqrt{\frac{2kT_{eff}}{m}}$$

(4-2) where k

is the Boltzman constant and m the molecular weight. Similarly, the most probable source velocity in the transverse beam direction is

$$\alpha_o = \sqrt{\frac{2kT_o}{m}}$$

(4-3)

Where T_o is the temperature of the gas in the nozzle. The flow velocity of the beam may then be defined by,

$$v_f = \alpha_o \left[\frac{\gamma}{\frac{2}{M^2} + \gamma - 1} \right]^{\frac{1}{2}}$$

(4-4)

Ideally, for an infinitely narrow beam distribution, the flow velocity is the peak velocity v_p. However, for a finit velocity distribution v_p is slightly higher than v_f.

Quantitatively,

$$v_p = \frac{1}{2} \left(v_f + (v_f^2 + 2n\alpha^2)^{\frac{1}{2}} \right)$$

(4-5)

Where n depends on the type of detector and beam used and is equal to 2 for a ground state particle detected by a number density detector. It is the peak velocities that are used to calculate the relative velocities.

The nozzles, both primary and secondary, are constructed of stainless steel(SS), with a 76μ nozzle diameter. Each nozzle may be resistively heated by passing current through a 0.01″ diameter Ta wire that is woven around it. Also each nozzle is surrounded by copper water lines to affect nozzle cooling. Nozzle temperatures are measured by room temperature reference thermocouples. After exiting the nozzle, the beams pass through a 0.6 mm diameter electroformed nickel skimmer situated eight mm downstream. The skimmer skims the outer fringes of the beam, collimating the jet, and prevents it from re-thermalizing with background gas.

4.1.2.   1°AND 2° BUFFER CHAMBERS

The 1° and 2° beams emerging from the skimmer, enter their respective buffer chambers. The primary buffer chamber produces the 2^1S and 2^3S He metastables by anti-parallel electron impact. Thermionic emission from a 0.1 mm diameter 1% thoriated tungsten filament biased at – 400V releases electrons which are then accelerated to 400eV by a grounded tungsten mesh(anode), 2-3 mm upstream from the filament. A set of four Mo pinch electrodes biased at – 500V confine electrons to travel into the He beam. A set of deflectors, which produce a field of 1kV/cm are placed at either end of this electron gun, They keep electrons from entering either the nozzle region or the scattering region. Emission onset requires a 1.5 A current across the

filament. To maintain a constant metastable production, a feedback circuit is used to hold the emission current at 0.1 A.

The 2^1S and 2^3S metastable He are produced in approximately 9:1, as measured by Stern-Gerlach experiments.[29] These are the two lowest excited states of He. The singlet is forbidden to radiatively decay to the ground state by $\Delta L = \pm 1$ selection rule. For triplets, the $\Delta S = 0$ selection rule also applies.

Optical quenching of one of the two metastable states is realized to perform state selected measurements, when needed. This is enabled by a He resonance lamp placed 0.5 cm downstream of the gun . The $2^1P \rightarrow 2^1S$ 2058 nm radiation emitted by the discharge quenches the 2^1S atoms via the transition $2^1S \rightarrow 2^1P \rightarrow 1^1S$ with the emission of 58 nm radiation ($2^1P \rightarrow 1^1S$). The 2^3S atoms are not quenched as this state is the lowest state of the triplet manifold.

After passing through the quench region, the metastable beam is collimated again by a 0.76 mm x 3.18 mm SS slit and enters the scattering chamber. The He* beam intensity is monitored by a faraday cup, placed in the main chamber, inline with the metastable beam. Metastable impact on the faraday cup SS electrode causes ejection of the secondary electrons and the resulting positive charge on the SS plate is measured by a picoammeter.

The secondary buffer chamber houses a tuning fork chopper mounted on the 2° differential pumping wall. A chopper frequency of 150 Hz. is used to modulate the target beam to a non-ambiguous background subtraction. Finally, the target beam is collimated by a 3 mm x 1.02 mm slit after which it enters the main chamber.

4.1.3.   DETECTION ASSEMBLY.

The metastable and target beams upon crossing (at a 90° angle) at the collision center produce ions which are extracted and focussed and finally detected by the Detection Assembly situated in the main chamber mounted on a rotatable lid allowing an angle scan between –7° to 100°, relative to the target beam. The angle scan is done manually with a sprocket-and-chain arrangement, The different detector components are   described below.

The first component of this chain, the Faraday Cage shields the collision volume protecting the ions from stray electrostatic fields which could alter, both, the velocities and deflection angles of the product ions. The cage is made of two duck-bill shaped SS plates with the 1cm gap between them covered by a grounded mesh. The plate and the mesh are coated with a thin layer of colloidal graphite (aquadag) to protect against surface charging. Condensation of pump oil on the Faraday cage could also lead to surface charging. This is avoided by using a pair of non-inductive resistors to heat the cage to 60°C.

4 cm downstream from the scattering center is a lens assembly, which consists of three retarder plates, followed by the three focussing SS electrodes. The ante-retarder, the first plate in the retarder series, has a 2.5-mm x 5.5-mm aperture. The next plate is the retarder, situated 3.25-mm away from the ante-retarder, has a 4.7 mm acceptance aperture covered by a SS mesh. The post-retarder lies another 3.25 mm away from the retarder with a similar size aperture . A thin layer of colloidal graphite is coated on all these components. The bias voltage applied to the focussing electrodes(each with a 9.5 mm diameter opening) is specified below.

The focussed and accelerated ions are directed towards a quadruple mass spectrometer(QPMS) which consists of four cylindrical SS rods, powered by a radio frequency

power source. The QPMS performs mass selection by filtering the product ions according to their mass- to-charge ratio. Ions exiting the QPMS are focussed by three lens electrodes into a Daly-type detector. The bias voltages for these electrode are 0.4kV, 4.0 kV and –0.4kV respectively.

The Daly detector is positioned at a 90° angle to the direction of the ions' path, and consists of a doorknob shaped Al cathode, biased at –25kV. The accelerated positive ions are attracted towards the cathode, causing an impact with subsequent emission of electrons. These secondary electrons are repelled downwards to reach the scintillator. The plastic scintillator is covered with a thin layer of Al, where electron impact produces scintillation, generating a stream of photons.

The photons are multiplied by the last component of the detection train, the photomultiplier tube(PMT). The PMT is biased at –1060V and provides a stable gain in excess of 10^7A vacuum feedthrough flange transmits the PMT output through an amplifier/discriminator (Ortec, Model 9302) and inputs it to the counting system. The data acquisition is described next.

4.2. DATA ACQUISTION

A complete experiment is comprised of two parts: an angular distribution (AD), followed by an energy analysis(EA).

In the AD mode of the experiment, first the QPMS is tuned to the mass of product ion of interest. The ante-retarder, retarder and post-retarder are all held at ground and the chopper is turned on. The detector is then placed at a certain angle and counts are collected for 10 seconds.

The detector can then be manually rotated to the next angle and the process repeated. At the beginning and the end of every scan, the detector is repositioned at a reference angle so that the AD data can be time normalized later. This reference angle is generally the angle with the peak signal or an angle very close to it. Typically, three complete scans for the entire range of angles are performed.

The output of the amplifier/discriminator is input into the counting system. The counter used in the AD mode is a dual-channel scalar (Jorway 1836), which is gated with the chopper. So when the chopper is open, both signal and background are collected in Channel A and when chopper is closed, only background is collected in Channel B . The counting system is interfaced to an IBM PC-XT computer. Thus the AD measures total production intensity at each lab angle for a given mass-to-charge ratio in the QPMS.

In the EA mode of the experiment, the retarder plate is ramped by a positive stopping potential. As this voltage increases from ground to the chosen positive value, the decrease in counts is observed. In this way, the translational energy distribution, that is, the velocity of the product ions scattered at each angle is measured.

The retarder plate in these experiments was ramped at a frequency of 90 Hz with a saw tooth waveform generated by a function generator. The ante-retarder was held at ground potential, the retarder at 0.6 V and the post-retarder was biased at −8V.
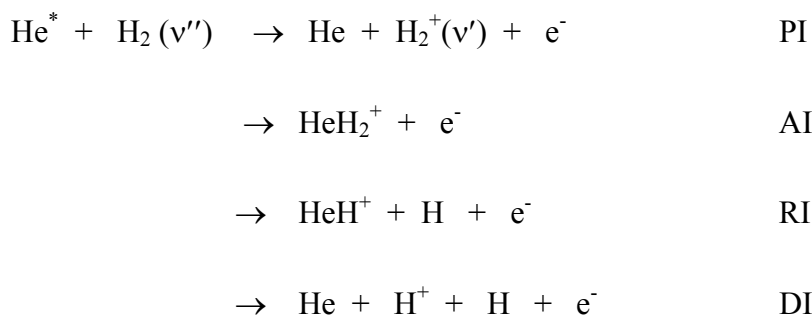
In the EA mode the amplifier/discriminator output is input into an ECL/TTL converter which produces a TTL pulse. The counter used for energy analysis is a data acquisition board run with multi-channel scalar (MCS) emulation software (EG&G-Ortec, Model ACEMBI). The TTL pulse is input into the MCS board. The MCS and the function generator are synched so that a function-generator-trigger, signals the MCS to begin counting. The number of channels chosen

was 100 with a dwell time of 100 µs in each channel. These choices were carefully made to avoid any overlapping between successive ramps so that the last channel finished counting slightly before the ramp ended. Also a pass count of 50,000 sweeps was used. The chopper was turned off during the energy analysis experiments to avoid time-synchronization problems with the MCS.

A retarding field spectrum was obtained for every angle measured in the **AD** mode.

5.   DISCUSSION

The system currently being studied is $\text{HE}^*(2^{1,3}S) + H_2$. An energy level diagram showing the relevant energies of this system is presented in Figure 5-1. The chemistry in a PI system involving a molecular target is more varied than in atomic PI. Four chemi-ionization pathways are energetically open for this system:

$$He^* + H_2(v'') \rightarrow He + H_2^+(v') + e^- \qquad\qquad \text{PI}$$

$$\rightarrow HeH_2^+ + e^- \qquad\qquad \text{AI}$$

$$\rightarrow HeH^+ + H + e^- \qquad\qquad \text{RI}$$

$$\rightarrow He + H^+ + H + e^- \qquad\qquad \text{DI}$$

Also in molecular PI, vibrational and /or rotational excitation of the target molecule needs to be considered, and spatial orientation of the target becomes important. Moreover, in the case of exoergic reaction, like PI, the question of energy disposal needs to be answered. Answers regarding energy transfer are most easily explored through PIAED studies. Results from angle- and velocity- resolved measurements of the H_2^+ intensity are discussed below.

A single collision-energy experiment was done which consisted of three separate trials to demonstrate reproducibility of the experiment. A room temperature(T= 50.2° C) helium beam was crossed with a hot (T= 420° C) hydrogen beam; this gives a collision energy of E= 3·1 kcal/mol. There are several steps on going from the raw LAB angular distribution and retarding

field spectra to the final result, the center of mass contour plot. Each step is described in sequence below.

Data reduction begins with a time-normalization treatment of the angular distribution data followed by quench lamp subtraction. The raw AD data comprises three angle scans from which data is time normalized and then averaged to yield one average signal at each angle.

Thus any fluctuations in the He^{*26} beam intensity and counting efficiency that might have occurred during the course of data acquisition can be adjusted. This is done by assuming that the reference signal varies linearly with time and so it can be linearly interpolated to give R(Θ), the reference signal for each angle in the scan. The time normalized signal at each Lab angle Θ is then determined by

$$S_N(\Theta) = S(\Theta) \cdot \frac{R_{av}}{R(\Theta)} \qquad (5a)$$

Where R_{av} is the average value for the reference signal over the course of the experiment, and S(Θ) is the unnormalized signal at angle Θ. Typical counting rates for the AD data range from > 1,000 counts per second at the peak angle to $\approx$ 20 count per second at the outer edges of the distribution. The AD background is generally 5 – 10 counts per second.

Quench lamp subtraction is then performed on the time normalized AD data, to isolate the triplet and singlet components of the angular distribution as,

$$2^1 S = \frac{(LOF - LON)}{q} \qquad (5b)$$

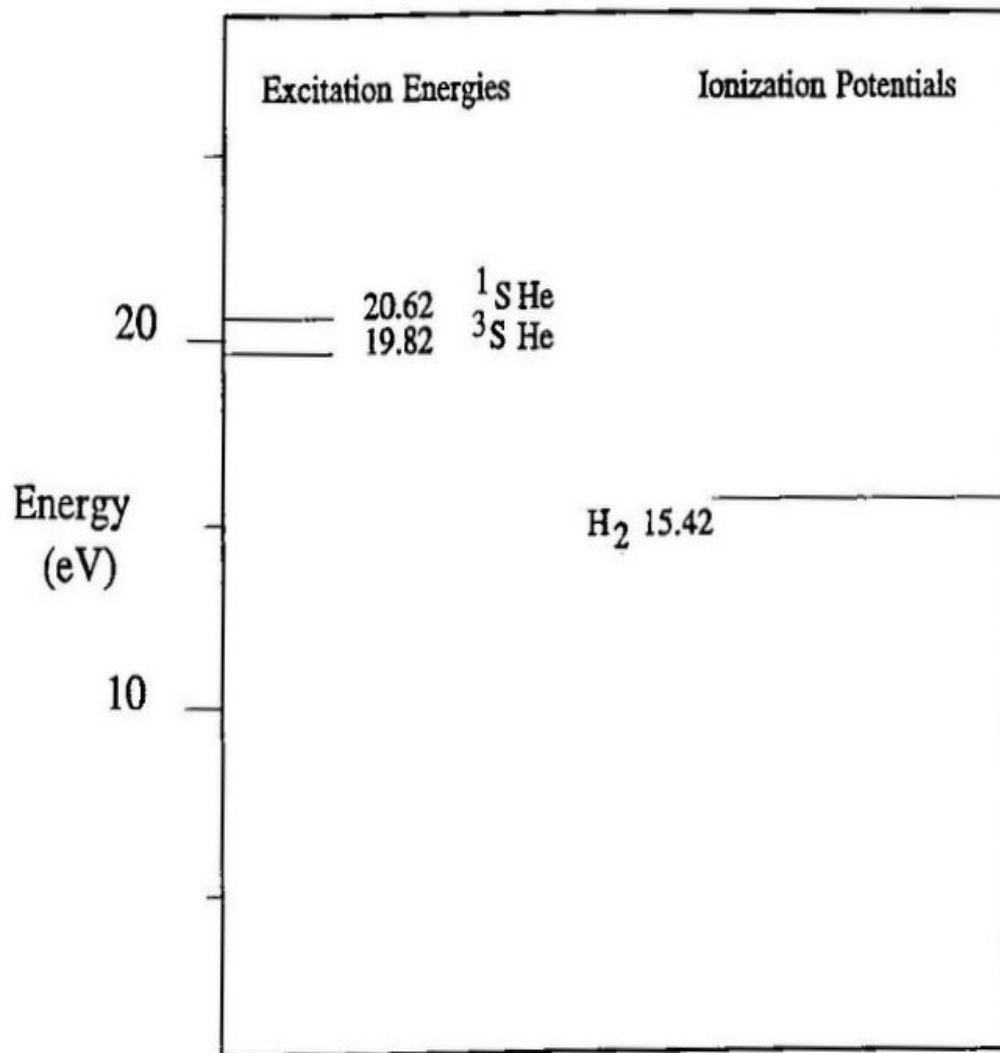$$2^3 S = \frac{LON - (1-q)LOF}{q} \qquad (5c)$$

Figure 5.1: Energy Level Diagram

where LOF and LON are the product ion intensity measured with resonance lamp off and on, respectively. The quenching efficiency, q, is typically on the order of 0.98, determined by previous experiments.[29]

Figure 5-2 shows a time normalized quench lamp subtracted angular distribution of H_2^+. A few qualitative features are evident from the plot. First, the LAB AD is very broad which, however, is largely a kinematic effect. Also at both small and large LAB angles, the intensity of the AD does not decline to zero. This is because at small angles the detector is physically limited to $\Theta > -7°$ because of the presence of the differential pumping wall between the 1° buffer chamber and the main chamber. At wide angles the AD was stopped before reaching negligible intensity because of charging problems as the detector neared the metastable beam. In Addition, the peak in the LAB is located to the small angle of the centroid angle, indicating forward scattering and a stripping mechanism.

The retarding field spectra are then each normalized near 0V retarding potential to the relative intensity at the corresponding angle. Each spectrum is then, differentiated to give the product energy distribution at that angle[23]. This is done by choosing some interval (within the 100 bins which comprise retarding field spectrum) around the point at which the derivative is being calculated. A Taylor series expansion is then performed on that chosen interval by means of a least squares procedure which gives the slope at that point. This procedure is repeated until the whole spectrum is differentiated. If a very large interval is chosen, the small peaks and inflections in the plot will disappear. Conversely, if the interval is too small, any noise in the spectrum will be carried over as a signal and might obscure the true structure of the differentiated spectrum. The same holds true for the choice on the degree of Taylor series used. A third order Taylor series was used and five channels were used as differentiation interval.
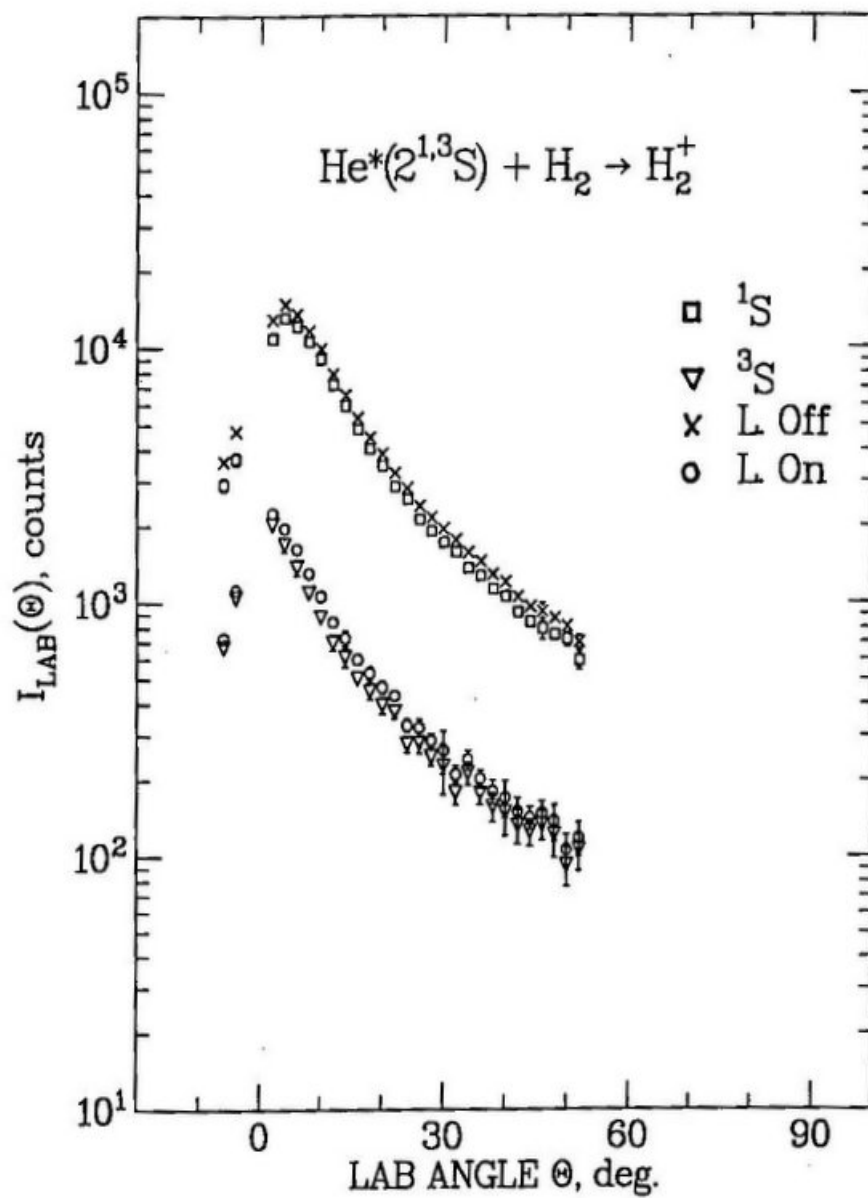
Figure 5.2: LAB angular distribution of H₂⁺ .

The product energy distribution is then transformed into a velocity distribution. This is done by converting intensity in energy space to intensity in velocity space using,

$$I(v) = I(E') \sqrt{2mE'} \qquad (5d)$$

Finally, LAB angles, velocities, and intensities are transformed into CM quantities generating a CM contour plot as shown in Figure 5-3. The plot maps H_2^+ intensity as a function of scattering angle and recoil velocity[24]. The contours represent the lines of equal relative intensity. Superimposed on the contour plot, is the most probable Newton diagram for the collision, which unveils the cause for the broad LAB AD. That is, the very small mass disparity between the reagents, give rise to a centroid angle of 46° yielding a broad distribution. Also the contours do not close at either large or small angles because of the incomplete AD, as described above. In Figure 5.5, the abrupt decrease in intensity at 90° is also a consequence of the same.

The sharply peaked behavior that was observed in the LAB angular distribution near 2° is also visible in the contour plot which corresponds to the maximum intensity. Surrounding the tip of the centroid vector is a valley which results from the u^2/v^2 Jacobian employed for LAB $\rightarrow$ CM transformation.

Also visible in the contour plot is a forward glory along CM 0°, corresponding to the peak intensity in the LAB angular distribution near 2°. This is a consequence of the forward scattering observed for this system. Figure 5-3 also shows that the velocity of the glory peak is slower than that of the incident H_2 beam. This indicates that the Penning H_2^+ ions were formed as a result of ionization from the repulsive portion of $V_0(r)$, over the well in $V_+(r)$.

The angle averaged recoil energy distribution(CMED) and the recoil energy averaged scattering angle distributions (CMAD) are presented in Figure 5-4 and Figure 5-5 respectively. These are obtained by integrating the doubly differential data plotted in the contour map. These
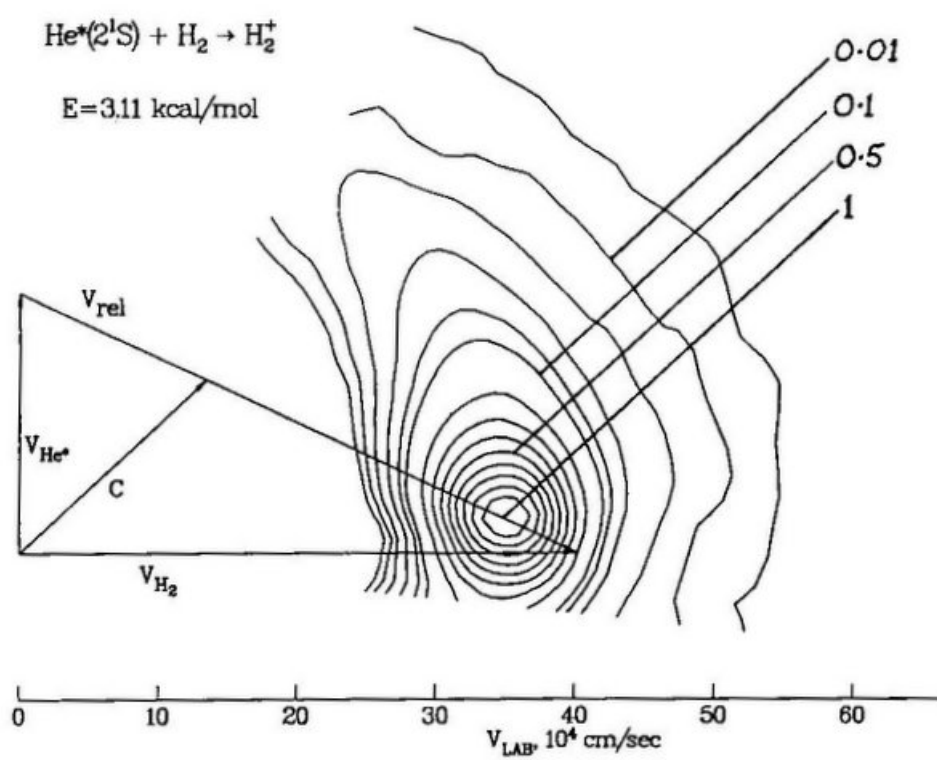
He*(2^1S) + H$_2$ → H$_2^+$

E=3.11 kcal/mol

0·01
0·1
0·5
1

V_{rel}

V_{He^*}

C

V_{H_2}

0   10   20   30   40   50   60

V_{LAB}, 10^4 cm/sec

Figure 5.3: Center of mass velocity-angle contour map of scattered H$_2^+$ for a collision energy of 3.1kcal/mol

plots present the same type of information, as in a contour map, but displayed in a different way and can help in the determination of individual effects of scattering angle and of recoil energy on the H_2^+ intensity.

Thus PIAED studies on molecular targets can yield a wide variety of qualitative information on molecular PI systems. Further experiments can help us probe deeper details on the dynamics of these processes as postulated in the proposed experiments listed in the following section.
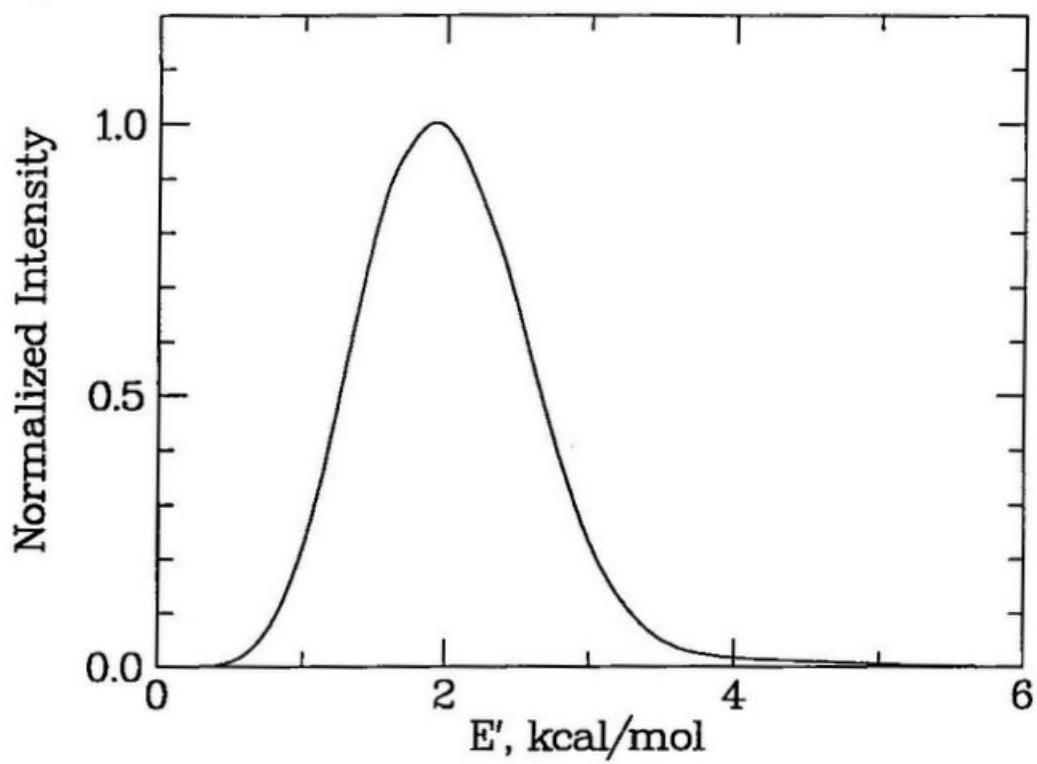
Figure 5.4: Center of mass recoil energy distribution of H_2^+, averaged over scattering angle (normalized to unity at the peak)
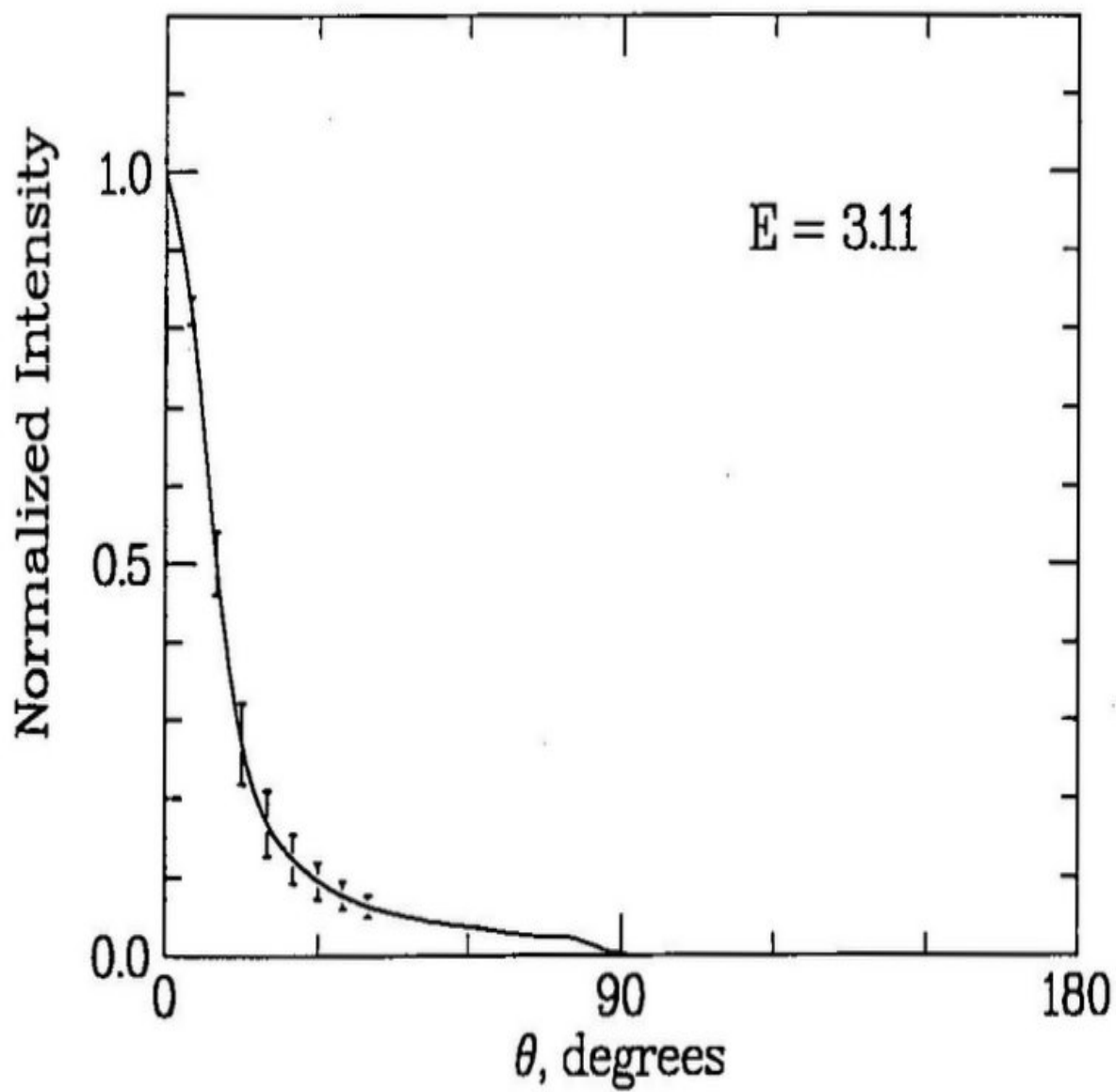
Figure 5.5: Center of mass angular distribution of H_2^+, averaged over recoil energy (normalized to unity at the peak).

6.   FUTURE WORK.

The preliminary H_2^+ data presented here, indicate the PIAED technique to be a powerful tool in the study of molecular PI systems. Although the data shown here are not conclusive, further experiments can be used to demonstrate the possibility of both the occurrence and detection of V$\rightarrow$T energy transfer in the post-ionization dynamics.

The immediate goal is to obtain reproducible RF data for series of collision energies for this same system. Collision energies can be varied by heating the secondary nozzle to different temperatures. In addition to PIAED studies of the H_2^+ ion, the HeH^+ rearrangement ion shows the promise of the use of PIAED to perform similar measurements. It presents an interesting example of nuclear rearrangement after ionization is over.

Longer terms plans include optimizing a second method of energy analysis, the time-of-flight (TOF) measurement of product ion velocity. Although this work is currently in progress, the detector sensitivity needs to be improved to obtain impressive data. Successful TOF may provide better velocity resolution. Further, since these data would be measured directly in velocity space, no differentiation may be needed. Considering the noise introduced by the differentiation procedure, this leverage of TOF method could prove quite beneficial.

An extension of molecular PI experiments to other diatomic targets (CO) is also planned. Also with the more sensitive energy resolution obtained by TOF method, the above mentioned intramolecular vibrational$\rightarrow$ translational energy transfer in the product ions can be studied. That

is, molecular Penning ions formed in a vibrationally excited state which experience $V \rightarrow T$ energy transfer before reaching the detector will be observed with a higher velocity compared to other molecular ions formed with the same initial kinetic energy which did not undergo this transfer. The vibrational progressions for these Penning ions have already been measured in PIES experiments on N_2, H_2, and CO done by Siska group (1995). These studies have confirmed that vibrationally excited product ions may indeed be formed.[25,26] Tuffin[27] (1989) also measured the velocity distribution of CO^+ produced by He^* PI, reporting such an energy transfer. But because of Maxwellian beams, his data are poorly resolved. Hence, experiments to obtain conclusive evidence to assertively answer this question, are planned using supersonic beams.

PIECES , Penning Ion/Electron Coincidence Electron Spectrum , studies are also planned as a long term prospect. These studies may provide the most detailed experimental view of the dynamics. The data will be ultimately used to approximate $V_0(r)$, $V_+(r)$, and Γ. To accomplish this, $V_0(r)$ is obtained from elastic scattering experiments and $V_+(r)$ is calculated. Thus modeling calculations of $I(\theta, E`)$ are necessarily a part of the immediate plans.

As the present work has shown, PI reaction dynamics still presents open questions and interesting challenges especially in case of molecular targets. However, the accomplishments thus far assure that new insight may be gained into the process.

BIBLIOGRAPHY

1. R.D. Levine and R.B. Bernstien, Molecular Reaction dynamics and Chemical Reactivity(Oxford, New York, 1987)

2. J.C. Polanyi, Science 236, 680 (1997)

3. G.C. Maitland, M. Rigby, E.B. Smith, and W.A. Wakeham, Intermolecular Forces: Their Origin and Determination(Oxford, New York, 1981), Chap 2.

4. M.F. Golde, Reactions of Electronically Excited Noble Gas Atoms in Gas Kinetics and Energy Transfer, Specialists Periodicals Reports, Vol 2 (The Chemical Society, London, 1977)

5. P.E. Siska, Rev. Mod. Phys. 65, 337 (1993)

6. P.J. Keliher, F.B. Dunning, M.R. ONeill, R.D. Rundel and G.K. Walters, Phy. Rev. A, 11 1271 (1975); L.G. Gray, R.S. Keiffer, J.M. Ratliff, F. B. Dunning and G.K. Walters, Phy. Rev. A 32 1348 (1985)

7. R.M. Jordan, D.W. Martin and P.E. Siska, J. Chem, Phys. 67, 3392 (1977).

8. D.W. Martin, R.W. Gregor, R.M. Jordan and P.E. Siska, J. Chem, Phys. 69, 2833 (1977).

9. P.E. Siska, Chem. Phys. Lett. 63, 25 (1979)

10. D.W. Martin and P.E. Siska, J. Chem, Phys. 82, 2630 (1985).

11. D.W. Martin and P.E. Siska, J. Chem, Phys. 89, 240 (1977).

12. A.L. Schmeltekopf and F.C. Fehsenfeld, J. Chem, Phys. 89, 240 (1977).

13. E.J. Longley, Ph.D. Thesis, University of Pittsburgh (1995).

14. C.E. Moore, Atomic Energy Levels, Vols. 1-3, (U. S. Govt. Printing, Washington D.C., 1949).

15. Lifetime for He (21S) from G.W.F. Drake, G.A. Victor and A. Dalgarno, Phys. Rev. 180, 25, (1969); for He (23S) from G.W.F. Drake, Phys. Rev. A 3, 908, (1971); all others N.E. Small-Warren and L. Y.C. Chiu, Phys. Rev. A 11, 1777(1975).

16. Polarizabilty for He (21, 3S) from G.A. Victor, A. Dalgarno, and A.J. Taylor, J. Phys. 1, 113, (1968); others from R.A. Molof, H.L. Schwartz, T.M. Miller, and B. Bederson, Phys. Rev A 10, 1131(1974).

17. H.M. Bevsek, D.C. Dunlavy, and P.E. Siska, J. Chem. Phys. 102, 33 (1995).

18. H. Nakamura, J. Phys. Soc. Japan 26, 1473(1969).

19. W.H. Miller, J. Chem. Phys. 95, 3371 (1991).

20. K.K. Sunil, J. Lin, H. Siddiqui, P. E. Siska, and K.D. Jordan, J. Chem. Phys. 78, 6190 (1983).

21. G.C. Maitland, M. Rigby, E.B. Smith, and W.A. Wakeham, Intermolecular Forces: Their Origin and Determination(Oxford, New York, 1981), Chap. 4.

22. T.T. Warnock and R.B. Bernstein, J. Chem. Phys. 49, 1878 (1968).

23. STUVELDS.FOR written by P.E. Siska.

24. IDORS.FOR written by P.E. Siska.

25. D.C. Dunlavy, D.W. Martin, and P.E. Siska, J. Chem. Phys. 93, 5347 (1990).

26. H.M. Bevsek Ph.D. Thesis, University of Pittsburgh (1996).

27. A.Le Nadan, G. Sinou, and F. Tuffin, Chem. Phys. Lett 156, 24 (1989).

28. J.B. Anderson, R.P. Andres and J.B. Fenn, Adv. Chem. Phys. 10, 275 (1966).

29. C.Weiser, Masters Thesis, University of Pittsburgh (1994).

30. C.Weiser, and P.E. Siska, Rev. Sci. Instr. 58, 2124 (1987).

31. D.C. Dunlavy, Ph.D. Thesis, University of Pittsburgh (1996).

32. H. R. Siddiqui, Ph.D. Thesis, University Of Pittsburgh (1985).

34. P.E. Siska, Comm. At. Mol. Phys. 15, 155(1984).